

7N-0.2-CR

12.27.89

p- 34

A GENERAL-PURPOSE TECHNIQUE
FOR TWO-DIMENSIONAL TRANSONIC FLOWS

SBIR 1983 Phase II

Gino Moretti
GMAF, Inc.
Freeport, NY

SBIR-02.01-8450

RELEASE DATE 12.27-89

Prepared for NASA Lewis Research Center
under Contract NAS3-24540
Final Report, December 1987

Project Summary

The NASA Contractor Report 3930 outlines a preliminary approach to the use of the λ -scheme, coupled with shock-fitting routines, for the numerical analysis of complicated two-dimensional, unsteady, inviscid flows. The present Report shows how the idea can be made practical, and a general-purpose code can be written, which contains all the shock-fitting procedures in a "black box", transferrable from one program to another, regardless of the complexity of the rigid wall geometries. Strong and weak shocks, both normal and oblique, in motion or steady, are properly detected and computed. The calculation is extremely fast and vectorizable. Examples of quite different nature are worked out and discussed.

Applications of the technique can and should be made to all two-dimensional problems with shocks, including intake and exhaust flows, cascades, single and multiple airfoils, store separation, etc. Three-dimensional extensions are anticipated.

(NASA-CR-194186) A GENERAL-PURPOSE
TECHNIQUE FOR TWO-DIMENSIONAL
TRANSONIC FLOWS Final Report
(GMAF) 34 p

N94-70498

Unclass

Z9/02 0183176

INTRODUCTION

The object of the present research has been the development of codes for the numerical analysis of two-dimensional (or axisymmetric), unsteady, inviscid flows of perfect gases within any range of Mach numbers where the polytropic assumption at a constant ratio of specific heats is valid. A special, but not restrictive, emphasis is put on internal flows (ducts, intakes, nozzles, and cascades).

Simplicity, accuracy and computational speed have been our goals. We have reached them by adopting a technique which departs from the common trend. We do not discretize the equations of motion in divergence form and we do not attempt to "capture" shocks as weak solutions of the partial differential equations.

Fitting of shocks agrees with their physical nature (in an inviscid model) as part of strong solutions. Their evaluation is very accurate and fast if the Rankine-Hugoniot conditions are used explicitly. An integration technique for ordinary points, based on the characteristic formulation of the partial differential equations, can be made to respect the concept of domain of dependence. In this way, the numerical procedure is simple and fast, and a high degree of accuracy is reached. Enforcement of boundary conditions and description of the shock environment are also possible without introducing arbitrary elements. The automatic separation of certain domains of dependence in the vicinity of the shock prevents the formation of wiggles and makes the use of arbitrary damping factors (artificial viscosity) unnecessary.

The integration technique for ordinary points is described in full detail in Ref. 1, a copy of which is attached to this Report. In particular, Section 7 contains all the formulas for a practical application of the technique to orthogonal grids (including Cartesian grids as a special case), and Section 8 does the same for H-grids. Section 9 presents the basic philosophy of shock-fitting, and Section 10 outlines the application of the idea to two-dimensional shocks.

TWO-DIMENSIONAL SHOCK-FITTING

In the present Report we expand Sections 9 and 10 of Ref. 1, in order to describe how the shock detection technique and the shock-fitting technique are actually coded. The ideas and procedures presented here supersede some of the content of Ref.

1.

A shock front is described by its intersections with grid lines. For brevity, we denote as x-lines and y-lines the two families of coordinate lines in the grid, whether they are Cartesian or curvilinear, orthogonal or not. The intersection of a shock with an x-line or a y-line is called an x-point or a y-point, respectively.

All information pertinent to shock points is stored in single arrays, depending on a counter, J. No attempt is made to organize the arrays; the shock points are stored at random, regardless of their relative positions in the physical plane. Cross-referencing between the grid points (denoted by an index N in the x-direction and an index M in the y-direction) and the shock points is necessary. To this effect, we use the following indices:

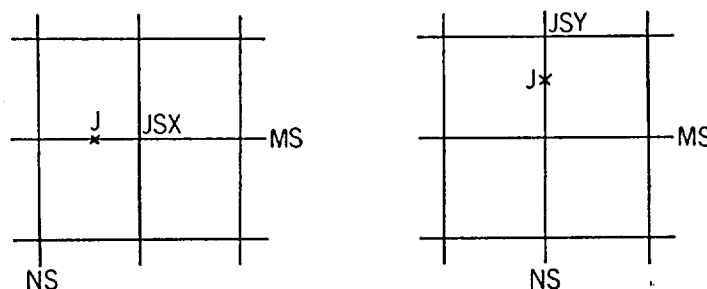


Fig. 1

NS(J) is the value of N to the left of an x-point or the value of N itself for a y-point (Fig. 1),
 MS(J) is the value of M for an x-point or the value of M below a y-point,
 JSX(N,M) is the value of J for the x-point lying on the Mth x-line to the left of the Nth y-line, and it is zero elsewhere,
 JSY(N,M) is the value of J for the y-point lying on the Nth y-line below the Mth x-line, and it is zero elsewhere,
 INDX(N,M) equals zero where JSX(N,M) equals zero, and 1 where JSX is not zero,
 INDY(N,M) equals zero where JSY(N,M) equals zero, and 1 where JSY is not zero,
 JI(J) equals 0 for an x-point with the high pressure on the left, 1 for an x-point with the high pressure on the right, 2 for a y-point with the high pressure below, and 3 for a y-point with the high pressure above.

In addition, the following arrays are defined:
 XS(J), YS(J) are the x- and y-coordinates of any shock point,
 ANGLE(J), for an x-shock, is the angle, α , between the normal to the shock at any shock point, and the x-line ($-\pi/2 \leq \alpha \leq \pi/2$),
 ANGLE(J), for a y-shock, is the angle, α , between the normal to

the shock at any shock point, and the y-line ($- \pi/2 \leq \alpha \leq \pi/2$),
 $W(J)$ is the normal shock velocity at any shock point,
 $TMA(J)$ is the absolute value of the normal relative Mach number
at any shock point.

To achieve a greater generality in two dimensions, Σ is no longer defined as in (83) of Ref. 1, but it is made depend on the velocity component normal to the shock, \tilde{u} :

$$\Sigma = (a_B + \delta |q_B - q_A|) / q_A \quad (1)$$

Therefore, (87) of Ref. 1 is replaced by

$$\Sigma = \frac{1}{(1+\delta)M} \{ [(\gamma M^2 - \delta)(1 + \delta M^2)]^{1/2} + \delta(M^2 - 1) \} \quad (2)$$

The relation between the time increments of Σ and M ($\Delta \Sigma$ and ΔM , respectively) is obtained from (2) as follows:

$$\Delta M = (1+\delta)\Delta \Sigma / \{ 2\delta + [2\gamma\delta M^2 + \gamma - \delta^2] [(\gamma M^2 - \delta)(1 + \delta M^2)]^{-1/2} - (1+\delta)\Sigma/M \} \quad (3)$$

Shock detection

Detection of x-points is performed first. Along any x-line, inflection points of λ_2 ($=u-a$) with increasing a , and all inflection points of λ_1 ($=u+a$) with decreasing a are marked. Indeed, Fig. 2 shows how coalescence of characteristics preludes to a possible formation of a shock. To reduce the effect of random oscillations in the distributions of a , the local variation in a , instead of being evaluated as $\Delta a = a_{n+1} - a_n$ or $\Delta a = a_{n+1} - a_{n-2}$, is evaluated as

$$\Delta a = a_{n+1} - a_{n-1} + 2(a_{n+2} - a_{n-2}) \quad (4)$$

This is equivalent to fitting the distribution of a with a straight line, approximating the actual distribution by the mean square rule, and using the slope of that line as the slope of $a(x)$ at x_n . A similar procedure is used to approximate $\Delta \lambda$ ($\lambda = \lambda_1$ or λ_2), and then the second difference, $\Delta_2 \lambda$, is obtained by subtracting $\Delta \lambda_{n-1}$ from $\Delta \lambda_n$:

$$\Delta_2 \lambda = -\lambda_{n+1} - \lambda_{n-2} - \lambda_{n-1} - \lambda_n + 2(\lambda_{n+2} + \lambda_{n-3}) \quad (5)$$

The cells where the inflection points are located are found where $\Delta_2 \lambda_n < 0$ and $\Delta_2 \lambda_{n+1} \geq 0$. Once such cells are marked, a tentative location for the shock is given by

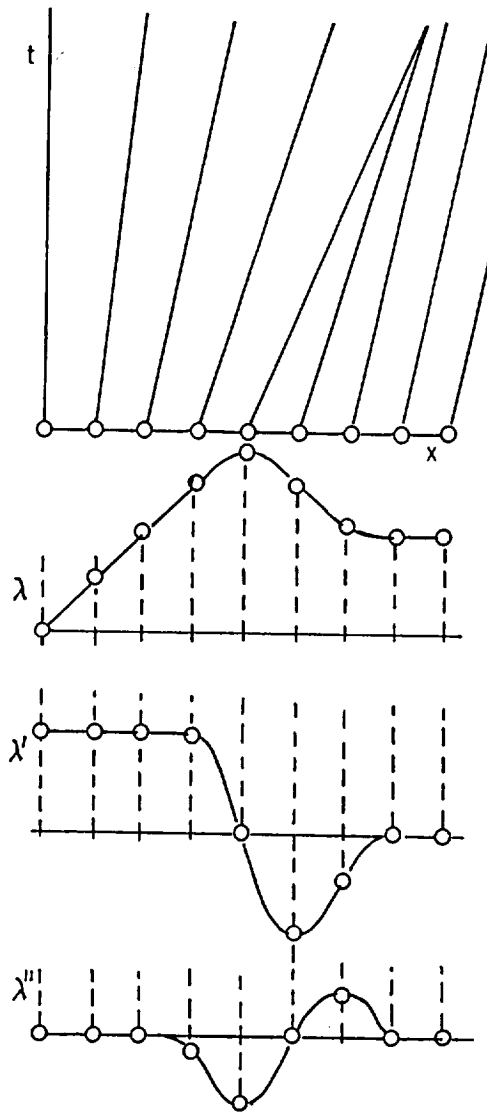


Fig. 2

$$x_s = x_n - \frac{\Delta_2 \lambda_n}{\Delta_2 \lambda_{n+1} - \Delta_2 \lambda_n} \Delta x \quad (6)$$

The point is not accepted as a shock point under three circumstances:

- 1) Σ , as defined by (1), is less than a prescribed tolerance, or
- 2) the pressure jump is too low, or
- 3) there is a shock point already in the cell or in any of the two adjoining cells.

The first criterion is used to discard "shocks" which have too low a relative Mach number; $\Sigma > 1.02$ is a reasonable

criterion, eliminating shocks which have $M < 1.03$. The second criterion is used to discriminate between shocks and contact discontinuities (as in the breaking of a diaphragm in a cylindrical pipe). Indeed, the criterion for λ may be satisfied, the speed of sound may change strongly in one cell, but pressure and velocity may remain practically the same. In this case, the discontinuity is not a shock but a contact discontinuity, but the test for Σ may be satisfied and the discontinuity accepted as a shock. The third criterion is used to avoid overcrowding of shock points. It is interesting to observe that the third criterion can be written in the simple form:

IF(JSX(N,M)+JSX(N+1,M)+JSX(N+2,M).NE.0)GOTO . . .

If the new shock point is accepted, JI is set equal to 0 or 1 according to the rule above. Then, a preliminary estimate of the shock slope at that point is made. With reference to Fig. 3, we define two neighborhoods of the new shock, J: the upper neighborhood, formed by the segments AB, CD, and EF, and the lower neighborhood, formed by the segments FG, DH, and KM. We search for other shock points on the upper neighborhood. The index, INDP, defined by

$INDP = INDX(N,M+1) + INDX(N+1,M+1) + INDX(N+2,M+1) + INDY(N,M+1) + INDY(N+1,M+1)$

equals the number of such shocks. If INDP differs from zero, the averages of the x- and y-coordinates of the shocks are evaluated. A single point, U, is defined as the upper neighbor of J.

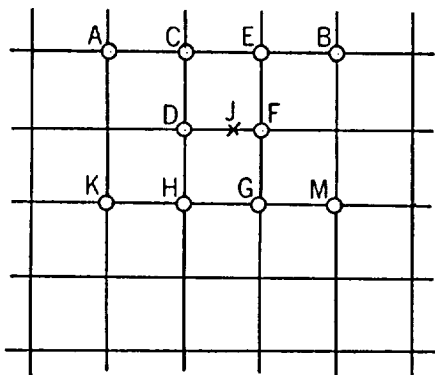


Fig. 3

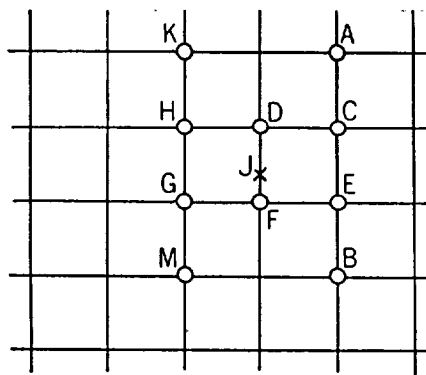


Fig. 4

The same procedure generates a lower point, L, if any shock point exists in the lower neighborhood of J.

If neither U nor L are found, the new shock point, J, is still isolated. The angle, α is set equal to 0.

If both U and L exist, the abscissa of J is corrected to be the average between the abscissas of U and L. Then, if only L exists, U is set equal to J; if only U exists, L is set equal to

J. If at least one neighbor exists, the angle α is defined from the coordinates of U and L, as the normal to UL and the x-line. By defining $L=-1$ if $Jl=0$ and $L=1$ if $jl=1$,

$$\alpha = \arctan [(x_U - x_L)/(y_L - y_U)] \quad (7)$$

The same procedure is repeated for y-points, working along y-lines. The above outline can be used, replacing u_{ia} with v_{ia} , x with y, JSX with JSY, increments and decrements of N with increments and decrements of M, and switching INDX and INDY with one another. The "upper" and "lower" points are now points to the right and to the left of the y-line, respectively. The index, JI, has to be set equal to 2 or 3 according to Δa being negative or positive. Fig. 3 is replaced by Fig. 4. Eq. (7) is replaced by

$$\alpha = \arctan [(y_U - y_L)/(x_U - x_L)] \quad (8)$$

Shock tracking

When the detection of new shocks is completed, the arrays providing the shock information may contain data pertaining to shock points already existing at the previous computational step, as well as data pertaining to newly detected points.

The first question to be answered is, Did any point, in its motion along an x-line or a y-line, cross over a line of the opposite family? To answer the question, a new value of NS is computed from the new value of XS for an x-point. If the new and old values of NS differ, not only NS is updated but some field values must be changed. Using Fig. 5, let the shock point, P move to a new position, Q. The flow values at A, which originally were pertinent to one side of the shock, are now pertinent to the opposite side; consequently, the code replaces them with the new values at B. Opposite action has to be taken if the shock point moves from Q to P; the values at A must be replaced with the new values at C. One proceeds in a similar way for y-shocks. Obviously, after checking the crossings, the distributions of JSX, JSY, INDX, and INDY are updated.

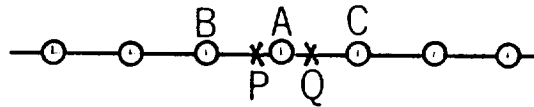


Fig. 5

Next, the entire array of shock points is checked, to eliminate possible duplications of shocks in the same interval. This is obtained by testing whether, for an x-shock, $JSX(NS(J)+1, MS(J))$ equals J or not. If it does, the J-shock is dropped. Similarly, the J-shock is dropped if it is a y-shock

and JSY(NS(J),MS(J)+1) does not coincide with J.

Then a search for neighbors of all shock points is performed again, as described above. All isolated shocks are dropped.

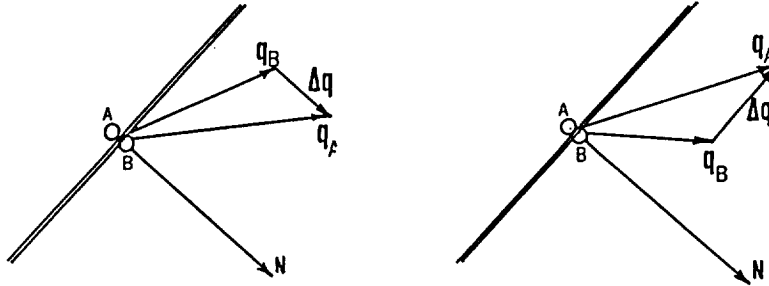


Fig. 6

For the others, the angles are defined by (7) and (8). Shocks whose angle is larger than 50° (in absolute value) are dropped.

Accidentally, a point may have been detected as a shock point when it belongs to a contact discontinuity instead. Both possibilities are shown in Fig. 6. On the left, there is a real shock. The difference, Δq , between the velocity vectors is normal to the discontinuity. On the right, there is a contact discontinuity, which is parallel to Δq . A contact discontinuity may be detected by our procedure described above. Consider for example, a case of two uniform, parallel flows such that the jumps in q and a satisfy the tests performed in detection. A pseudoshock is found but if we computed $\Delta q \cdot N$, the result would be identically zero. In practice, we are bound to test Δq using nodes bracketing the alleged shock; due to the uncertainty of the numerical approximation, we cannot eliminate pseudoshocks only if $\Delta q \cdot N = 0$ but also when the cosine of the angle between Δq and N is sufficiently small. An "x-shock" is then dropped if

$$|\Delta u \cdot N_1 + \Delta v \cdot N_2| < \kappa |\Delta q| \quad (9)$$

and a "y-shock" is dropped if

$$|-\Delta u \cdot N_2 + \Delta v \cdot N_1| < \kappa |\Delta q| \quad (10)$$

where κ is, for example, .5.

At this stage we have all the ingredients needed to define Σ , according to (1), at all shock points. Note that $|q_B - q_A|$ of (1) is defined by the left-hand sides of (9) and (10) for x-shocks and y-shocks, respectively. All points having $\Sigma < 1.02$ are dropped. Then, M is evaluated as a function of Σ using (2). These values are obtained at the end of every computational step and are needed in the following step to update M , the shock

velocity (W) and the shock position at every point.

Shock calculation

The shock points are updated after all grid points have been updated. New grid values of a and q are picked on either side of the shock, at two nodes bracketing it (for an x-shock, at nodes lying on the same x-line; for a y-shock, at nodes lying on the same y-line). Using such values, the left-hand sides of (9) or (10), and (1), a new value of Σ is found at each shock point and $\Delta\Sigma$ is determined by subtracting the corresponding Σ at the end of the previous step. Then (3) provides ΔM and the problem is solved.

Once the normal relative Mach number is found, indeed, the Rankine-Hugoniot equations [(13) of Ref. 1] are applied to update the point on the high-pressure side of the shock. The shock velocity, W , is computed from

$$W = q_A \cdot N \pm a_A M$$

where q_A and a_A are evaluated on the node next to the shock on the low-pressure side. The + sign holds for $JI=0,2$ and the - sign for $JI=1,3$. Note that

$$W = u_A N_1 + v_A N_2 - \kappa a_A M \quad (12)$$

for an x-shock ($\kappa=-1$ if $JI=0$, 1 if $JI=1$), and

$$W = -u_A N_2 + v_A N_1 - \kappa a_A M \quad (13)$$

for a y-shock ($\kappa=-1$ if $JI=2$, 1 if $JI=3$). The shock location is updated by adding $W/N_1 \cdot \Delta t$ to the abscissa of an x-shock or to the ordinate of a y-shock.

Special treatment at grid nodes neighboring shocks

Nodes in the immediate neighborhood of a shock point must be detected because approximating derivatives by differences between nodes on opposite sides of a shock must be avoided.

For an x-shock, such as J in Fig. 7, the points A and B are considered first. Two subroutines, $FXM(N,M,JSX(N,M))$, and $FXP(N+1,M,JSX(N+2,M))$ are called, where $N=NS(J)$, $M=MS(J)$. The first deals with point A, the second with point B. If the third index in their calling sequence is different from zero, another shock point exists in AG or BQ, respectively. In that case, all f_1^x are set equal to zero (the flow is assumed not to change between the two shocks). Otherwise, at A, any f_1^x with a negative coefficient is approximated using differences taken between A and G; at B, any f_1^x with a positive coefficient is approximated using differences taken between Q and B.

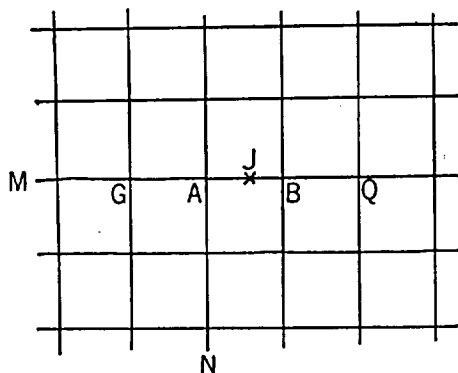


Fig. 7

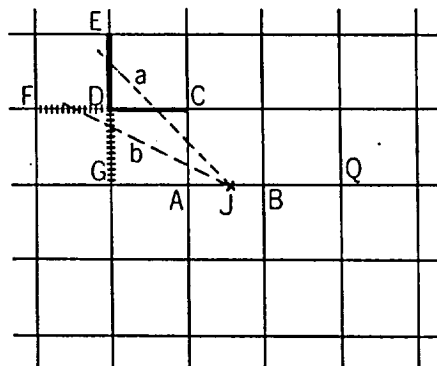


Fig. 8

Continuing our analysis of x-shocks and moving to Fig. 8, we must consider the possibility of shock waves located as the oblique line issuing from J. An index, ILL, is defined as

$$ILL = INDY(N-1,M) + INDY(N,M) + INDY(N+1,M)$$

and then the following statement is used:

```
IF(JSX(N,M+1)+JSY(N-1,M+2).NE.0) CALL FYM(N,M,JSX(N,M-1),ILL,0)
```

The test detects shocks on the CDE line; in this case, in computing A, differences to be taken between C and A are taken between D and A instead, unless $ILL \geq 2$ (in which case a y-shock crosses the DA line and differences are set equal to zero).

The same analysis, with obvious changes, is repeated in the other three quadrants around J. For a y-shock, the entire procedure is easily modified by interchanging x and y, and N and M.

APPLICATIONS

Applications of the technique have been made, so far, to test the dependability of the shock-fitting routines, their robustness and the possibility of shaping the entire shock-fitting technique as a black-box for general purposes (the major objections raised against the λ -scheme and shock-fitting, indeed, have been that such techniques have only a limited reach and require a skilled personal intervention every time a new problem is to be studied). Two applications have been made using H-grids. In these cases, however, only x-shocks have been considered. Four more cases have been studied, containing both x-shocks and y-shocks. Two of these cases have been treated using Cartesian grids and one using a curvilinear orthogonal grid.

Transonic flow in a duct

The interest of the problem lies in the appearance of oblique shocks in supersonic flows. Such shocks tend to become steady, if the oncoming supersonic flow is steady. According to the geometry of the duct and the upstream Mach number, however, the shocks may be reflected regularly or produce a Mach reflection. Details of the latter case are shown in Figs. 9 through 15. The duct has a constriction, produced by a straight wall at a 20% slope. The upstream flow is uniform, with a Mach number equal to 1.6. The calculation is started impulsively, by distributing uniform values at all grid points, except along the oblique wall. Such an impulsive start is representative of the rapid acceleration of the duct from right to left, starting at a state of rest and reaching a cruising velocity at $M=1.6$. Numerical experiments performed with different, high but finite accelerations showed that, as soon as the cruising speed is reached, the flow field is not radically different from the one obtained assuming an impulsive start.

Fig. 9 shows isomachs at a preliminary stage (obtained using a 100x30 mesh). An oblique shock is forming at the origin of the oblique wall. In the vicinity of the corner, the shock is practically steady and it has the correct angle for an oblique, steady shock in a supersonic flow. Note that, despite the weakness of the shock, the correct angle could not be obtained without shock-fitting. A shock of this type, captured by the λ -scheme, would be wrong by about 3° . In Fig. 10 the oblique shock has extended almost to the bottom wall, and a reflected locus of higher pressure gradients (not a shock yet) begins to show. In Fig. 11 the oblique shock is apparently producing a regular reflection. Such a pattern, however, is not stable. The oblique shock is not straight; its strength decreases towards the bottom wall and a regular reflection is, for a short time, physically possible.

As the strength of the oblique shock increases, a Mach reflection must appear, followed by a region of subsonic flow. This new phase of the evolution is shown in Fig. 12 (which, as the following figures, has been obtained using a 150x30 mesh). It is worth noting that the transition from a regular reflection to a Mach reflection occurs smoothly as the calculation proceeds, without any need for external intervention or special codings.

As the subsonic region increases in size, the Mach stem is pushed upstream (Fig. 13). Step-by-step movies of the calculation show that the upstream motion starts at the triple point and propagates downwards. Eventually, the reflected shock itself is followed by a subsonic region; its upper point reaches the end of the oblique wall and continues moving upstream (Fig. 14). The calculation is interrupted when the Mach disc has swallowed the entire original oblique shock and a straight shock remains, pushed upwards by the subsonic region in a uniform

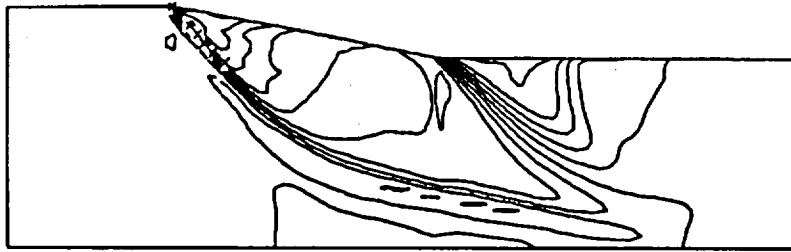


Fig. 9

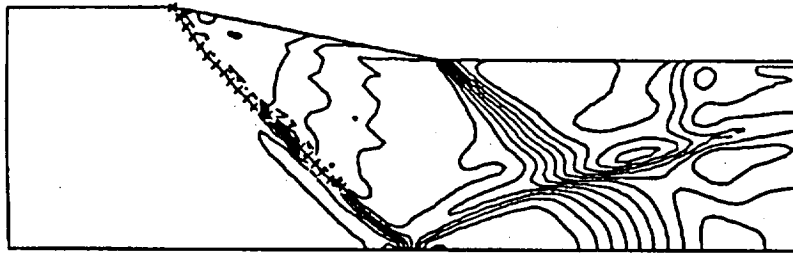


Fig. 10

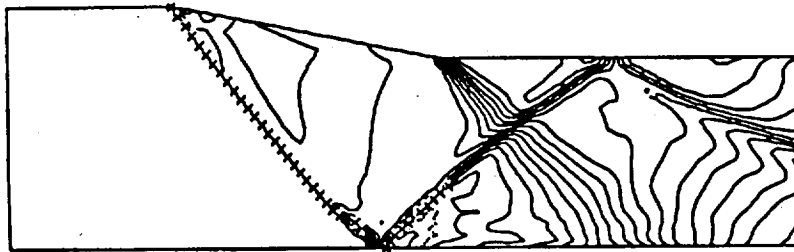


Fig. 11

motion (Fig. 15). In the right portion of the duct, expansion waves and recompression shocks are visible.

The appearance and disappearance of weak oblique shocks and strong, almost normal shocks is well controlled by the code, as well as the local behavior and motion of the triple point and the transition from regular reflection to Mach reflection. The entire calculation takes about 50 seconds on a CRAY X-XMP with a 150x30 mesh.

With minor alterations, the same program can be used for the analysis of flows in ducts of different geometries (not necessarily with a straight bottom wall). Moreover, a given geometry may be rotated by an arbitrary angle, still maintaining

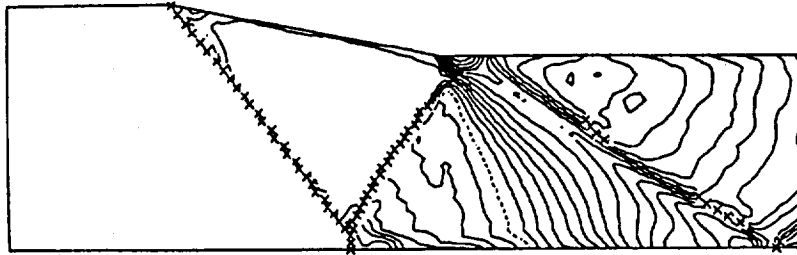


Fig. 12

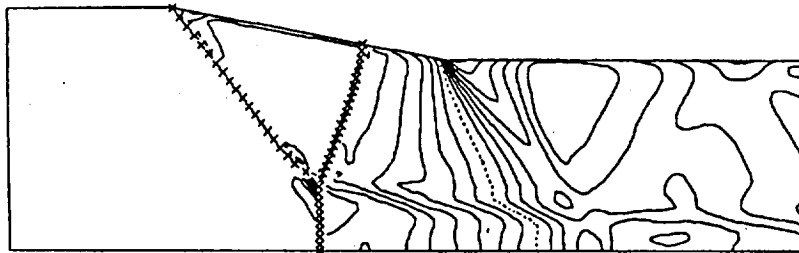


Fig. 13

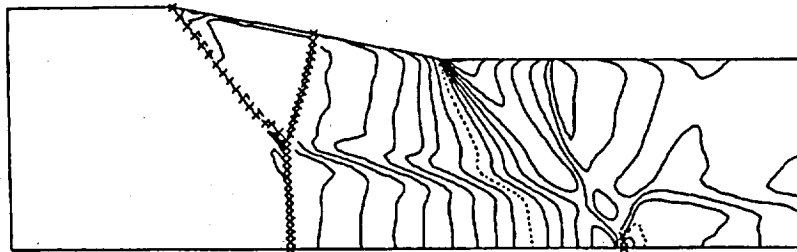


Fig. 14

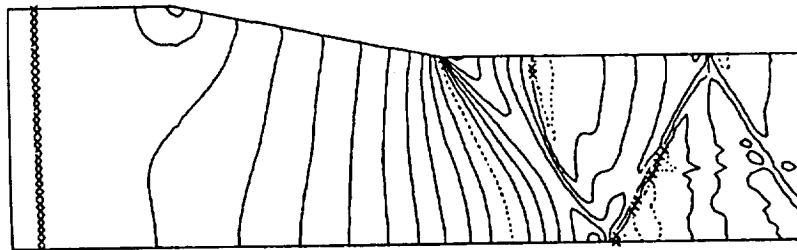


Fig. 15

one family of lines in the H-grid parallel to the original y-axis. For example, Fig. 16 shows the H-grid for the same geometry of Fig. 9, when the duct is turned 30° counterclockwise. Such a device may allow a calculation to be made for a staggered cascade, still keeping a set of grid lines normal to the cascade axis. This may be important to simplify eventual extensions of the technique to quasi-three-dimensional analyses of cascades.

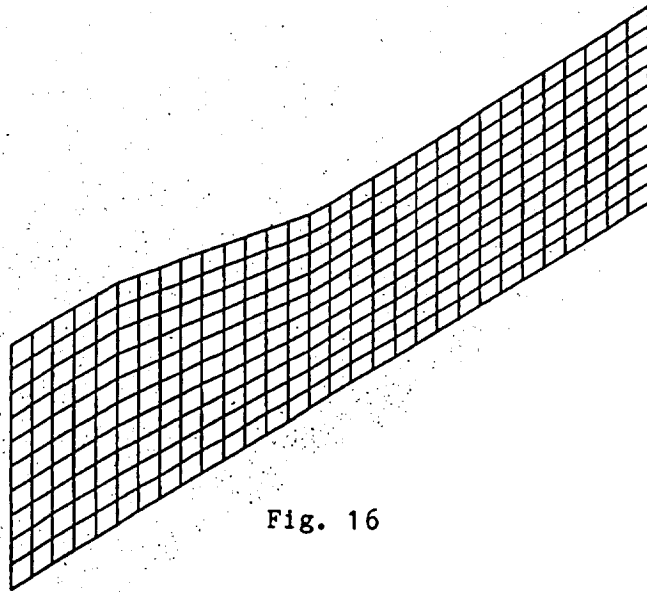


Fig. 16

Intakes

To analyze the flow within and around a two-dimensional intake, of a shape similar to the one shown in Fig. 17, we employ a variant of the program used for inner flows in ducts. The intake may have a non-rectilinear bottom wall (which extends in front of the intake for an arbitrary length); the cowl lip must be sharp. The geometry shown in Fig. 17 was suggested in 1984 by a GAMM panel for a Workshop on computational techniques, to be held in Paris in June 1986 (Ref. 2). Despite the eventual appearance of some French results after the Workshop, it is worth noting that our work reported here provided the sole clean results at Workshop time.

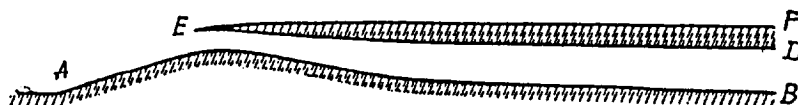


Fig. 17

Our program works on two H-grids. The lower one is limited by the bottom wall, the upper wall inside the intake, and a straight horizontal line issuing from the cowl lip. The same straight line, together with the outer wall of the cowl, is the lower boundary of the upper grid, whose upper boundary is another straight horizontal line, located at an arbitrary distance from the intake. The vertical grid lines are equally (and evenly) spaced in both grids. The other grid lines are stretched by the geometry in the physical space; in the computational space, their Δy are constant in each grid, but different from one grid to the other (Fig. 18).

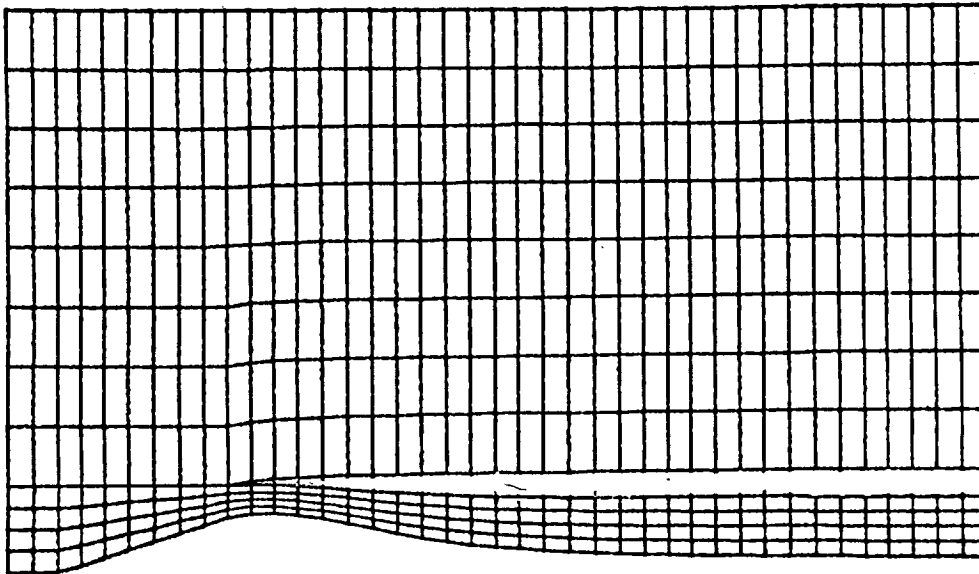


Fig. 18

In each grid, the computation proceeds as described above. The only novelty here is in the matching of the grids. In the outer grid, f_1^y is unknown; in the inner grid, f_2^y is unknown. In addition, according to the sign of v , f_3^y and f_4^y are unknown either in the outer grid (if $v > 0$) or in the inner grid (if $v < 0$). In conclusion, four unknowns have to be determined at every point common to the two grids; such unknowns are computed from Eqs. (64) through (67) of Ref. 1, by matching the time derivatives of a , u , v , and S , considered as pertaining to the inner grid or the outer grid.

For the GAMM Workshop, two problems were proposed:

- 1) a case with $M_\infty = 2$ and $M_e = 0.27$, which should produce an oblique, attached shock at the inlet bottom wedge and a detached shock in front of the cowl, resulting in a λ shock configuration, and

2) a case with low free stream Mach number, $M_\infty=1.2$ and a prescribed value of M at the engine ($M_e=0.3$), which should produce a weak, but practically normal, shock at a large distance from the intake.

We started our computations by distributing free stream values over both computational grids, except within the intake, where the Mach number was assumed to decrease linearly from M_∞ to M_e and v was adjusted on the walls to make the normal velocity component vanish.

In the first case, the computational region is limited by $x=-15$ to the left and by the intake exit to the right, by the bottom wall and by $y=40$. The grid has 150 intervals in the x -direction, 15 intervals across the intake and 45 intervals above the cowl. Results for this calculation are presented in Figs. 19 through 25. An oblique shock is generated by the wedge to the left of the intake, and slowly grows and straightens up within the free stream. A normal shock appears within the duct and moves towards the intake throat, acquiring strength. A third oblique shock is generated by the cowl lip and soon detaches itself. The flow pattern in front of the intake after 300 steps ($t=41.8$) is shown in Fig. 19; the shock inside the duct is not visible. After 800 steps ($t=116.19$) the pattern has changed as shown in Fig. 20; here we also see the normal shock, shortly after it reaches the throat. At this stage, the latter slows down and loses strength, until it disappears altogether (Fig. 21). The shock pattern remains well stabilized rather soon; the flow within the intake, however, takes a long time to become steady. Even after 6000 steps, minor waves still move back and forth through the intake, carrying information from the exit boundary (prescribed Mach number) all the way to the entrance, and reflecting it at the lip shock. The stabilization of the flow in the intake is well described by a history of the mass flow. The mass flow is computed by integrating ρu by a trapezoidal rule between the bottom boundary and the coordinate line reaching the cowl lip, followed by the upper wall of the intake. The mass flow is obviously going to be constant until part of the gas spills above the line; after reaching the entrance section, the mass flow should remain constant again, at a lower level. So long as the flow is unsteady, the mass flow is not constant. In particular, if there is a shock moving to the left, the mass flow behind the shock is smaller than in front of it; if the shock moves to the right, the mass flow increases across the shock. Part of the mass flow history during 6000 computational steps is presented in Fig. 22. At the beginning, very large waves appear in the intake. Minor wiggles in the graph, to the left of the section where the spillage begins, are a defect in plotting; the mass flow is computed, as we said, by a trapezoidal rule of integration, disregarding the presence of the oblique shock. The last plot of mass flow shows a practically constant value all along the intake. Figs. 23, 24 and 25 show the distributions of M , C_p and S over the walls of

the intake. Note the jump in entropy at A, across the first oblique shock, and a second small jump on the bottom wall, across the second shock. The entropy at E is much larger, because of the higher strength of the second shock in its vicinity. As a consequence, the Mach number on the upper wall of the intake (ED) is lower than on the lower wall (AB), except at the exit, where the Mach number is prescribed. A movie of the evolution of the shock pattern, until a steady state is reached, is available.

The second case needed a very high upper grid, because the bow shock tends to an almost vertical position and it is hard to impose correct boundary conditions behind it when it reaches the upper boundary. Even using the grids extended over the regions shown in Fig. 26, we could not reach a steady solution, since the root of the shock still moves slightly to the left when spurious disturbances start propagating downwards from the intersection of the bow shock and the upper boundary. A plot of constant Mach lines at the end of the computation is shown in Fig. 27. The standoff distance history is given in Fig. 28. The solid line is actually computed; the broken line is a guess of what the standoff distance would be if the computation were continued in a taller region. The final mass flow distribution (as defined for the first case) is given in Fig. 29. A slow decrease in mass flow follows the bow shock, because of an increasing upward deflection of the subsonic flow at the upper grid line. Conversely, the mass flow through the intake is perfectly constant, except for a slight jump at the location of the shock inside the duct, because the shock is not perfectly stabilized yet.

Complex Mach reflection

The applications described above used a set of routines considering x-shocks only. Generalization of the procedure to flow fields for which both x- and y-shocks must be treated was tested in the following problems.

Firstly, we considered a problem which has been extensively discussed by Woodward and Colella (Ref. 3), the complex Mach reflection of a normal shock on an oblique wall. We use the same Cartesian grid as in Ref. 3, although with fewer points. The impinging shock has a Mach number of 10, so that the Mach number of the flow behind it is 1.83. The impinging shock forms an angle of 60° with the wall. The grid is parallel and orthogonal to the wall. With the given data, the reflected shock cannot be attached to the wall, but we force it to be, to match the assumptions of Ref. 3. The flow is self-similar; our calculation, however, begins when the impinging shock has just cleared the leading edge of the wall. We must let the pattern develop and we expect to reach self-similarity only after a reasonable resolution has been obtained. The main features of this case of complex Mach reflections are: (1) the impinging

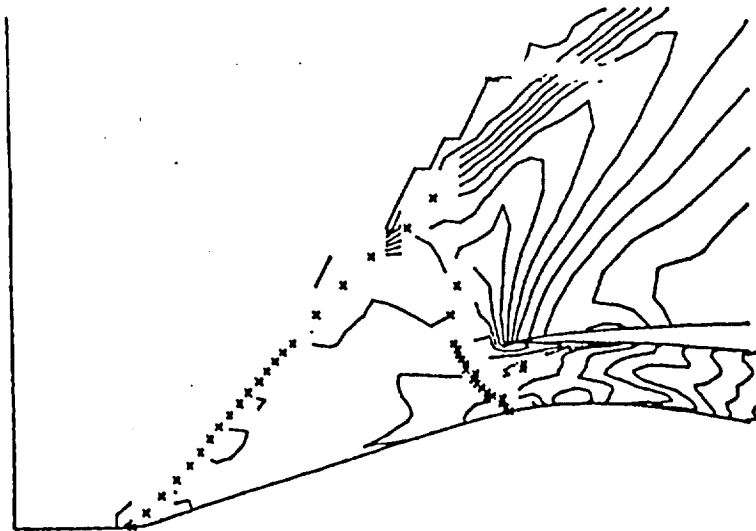


Fig. 19

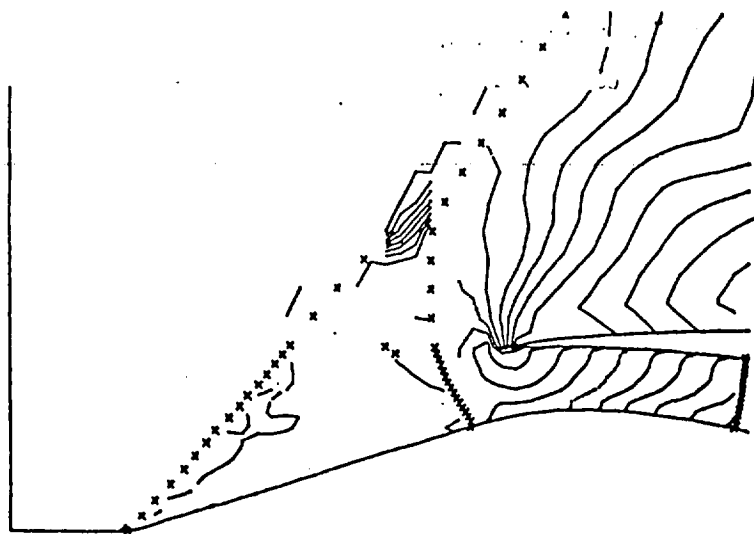


Fig. 20

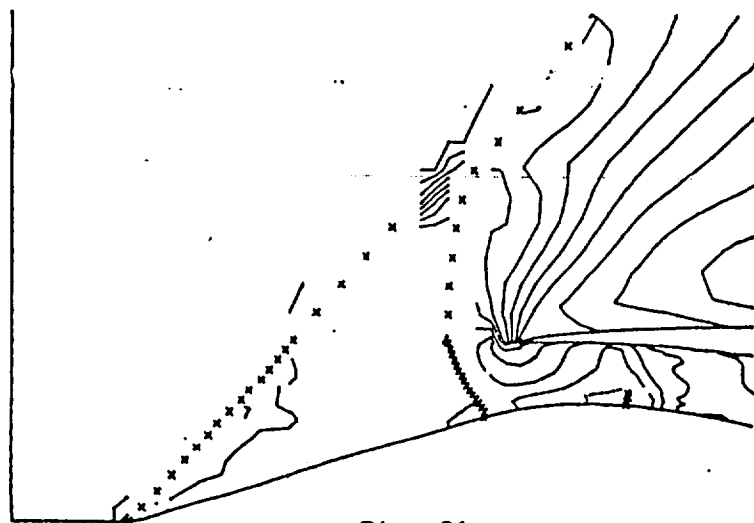


Fig. 21

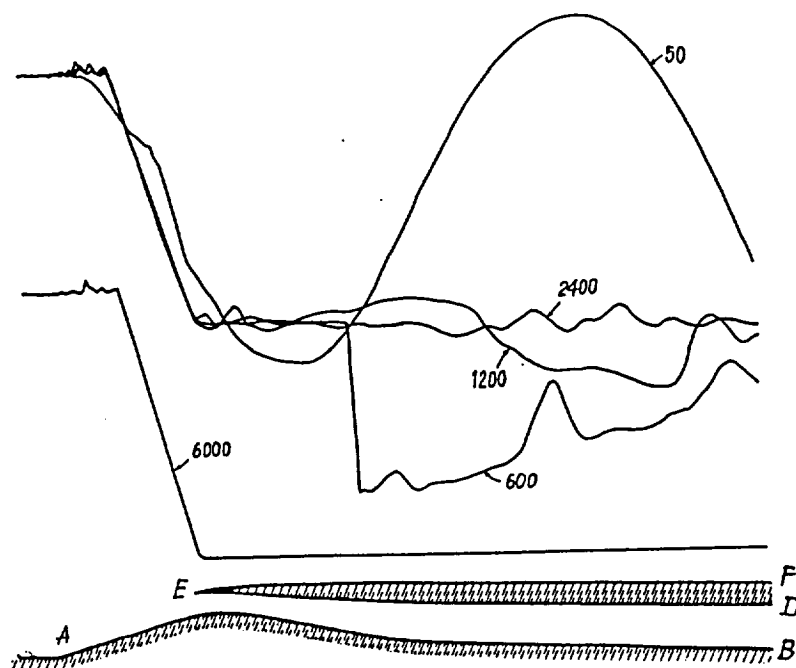


Fig. 22

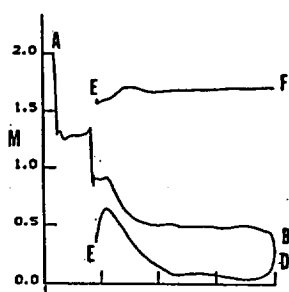


Fig. 23



Fig. 24

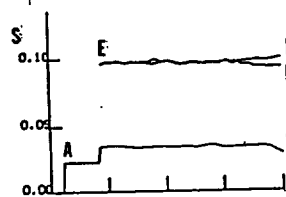


Fig. 25

shock, moving at a high speed into a gas at rest, and leaving behind a region of supersonic flow and high pressure (this is a novel case of subsonic-to-supersonic transition), (ii) a Mach stem, moving even faster and growing in height, (iii) a curved shock, beginning at the leading edge of the wall and practically normal to it, which turns into a shock parallel to the wall, (iv) a kink in the curved shock, followed by a short, weak shock ending in a triple point on the impinging shock, (v) a contact discontinuity stemming from the triple point and reaching the wall, (vi) an extremely weak shock stemming from the kink and

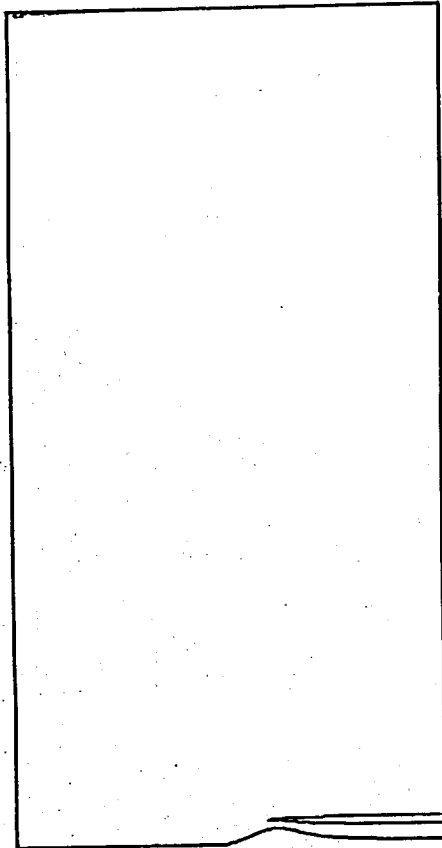


Fig. 26

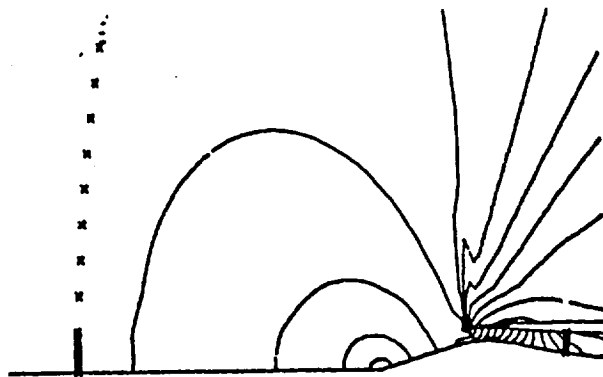


Fig. 27

pointing towards the contact discontinuity. In our calculation, no attempts have been made to fit the contact discontinuity; the shocks, however, have all been fitted. This problem requires the complete fitting technique, for shocks oriented in any direction. Typical results are shown in Fig. 30 ($\ln p$, $\ln p$, S , $u-13.6626$, and v). Our results should be compared with Fig. 4 of Ref. 3. Note in particular that our plot of $u-13.6626$ has to be compared with their plot of $vx-11.547$; the difference in the subtractive constant is due to a different scaling of velocities. Symbols for the fitted shocks are not shown in Fig. 30 (they are too large and the shock points are too close to one another; they would produce a wide black band without allowing

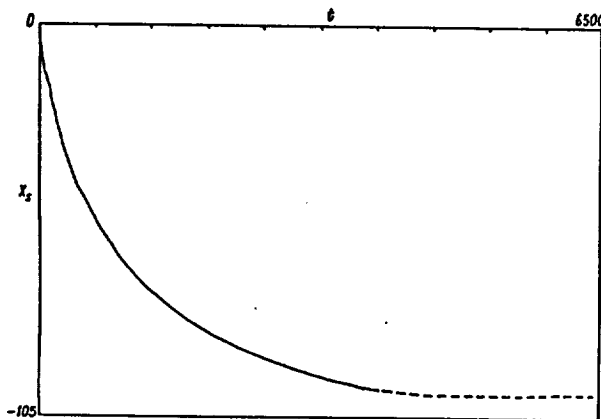


Fig. 28

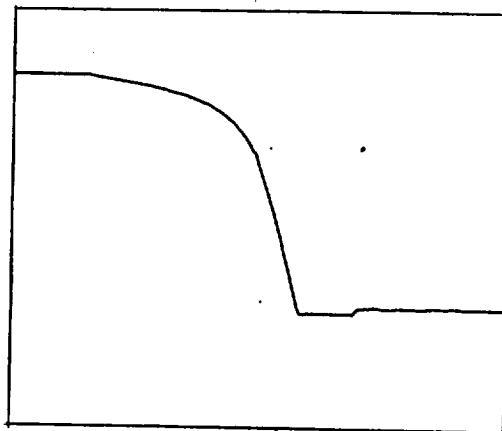


Fig. 29

points of different nature to be differentiated). Consequently, the plots look like the ones obtained by shock-capturing techniques. The comparison with the best results of Ref. 3 is excellent. The entire calculation takes about 69 seconds for 523 steps on a CRAY-XMP computer.

In the following figures, Figs. 31 through 36, plots of constant Mach number lines at different steps are presented, all scaled in a self-similar fashion. At step 50 (Fig. 31), the perturbed region is confined to a 30x6 mesh; the resolution is extremely poor. Nevertheless, the impinging shock and the Mach stem are well defined, and so is the arched portion of the refracted shock. The lack of resolution is noticeable particularly in the right portion of the perturbed region. At step 100 (Fig. 32), the perturbed region is covered by a 57x11 mesh. With increasing resolution, the number of fitted shock points increases, generating continuous shock lines. Note that J_1 equals 0 at points marked by circles, 1 at points marked by crosses, and 2 at point marked by triangles. Yet, the right-hand side of the figure leaves much to be desired. In Fig. 33, the pattern at step 150 is shown without the mesh, for clarity. The mesh covering the perturbed region is now 83x16. Note the appearance of three x-shocks with $J_1=1$ at the extreme left. Note also the increase in details at the right. Finally, see in Figs. 34, 35, and 36 the continuing improvement in details at steps 200, 400, and 520, where the meshes contain 100x20, 168x38 and 208x49 cells, respectively. In the last figure, the shock fronts become a thick blur; if the circles, crosses and triangles are removed, Fig. 37 results where, once again, the plot takes on the typical aspect of a plot obtained by applying a

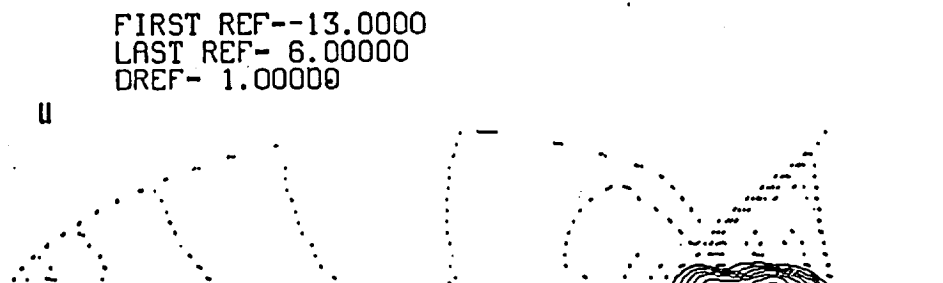
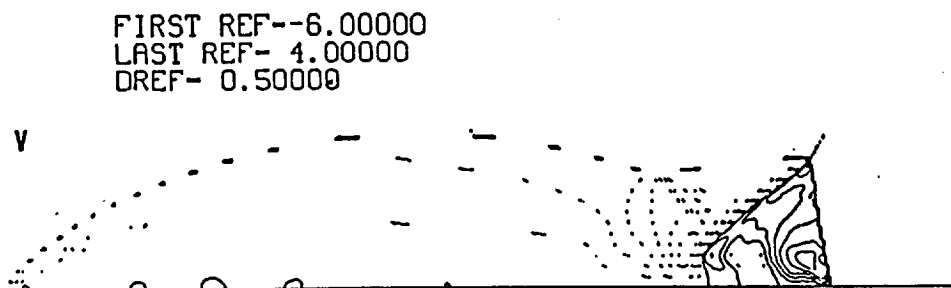
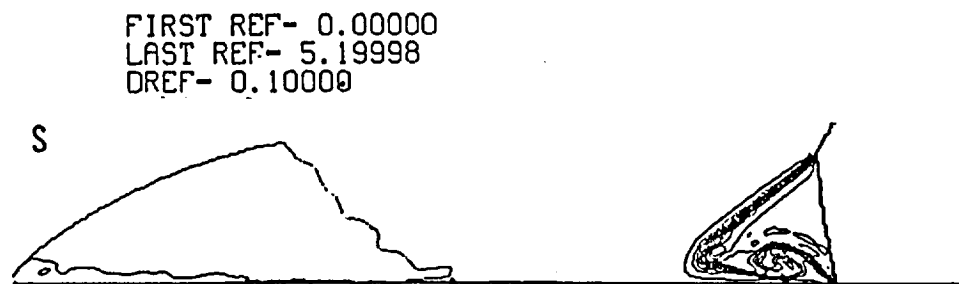
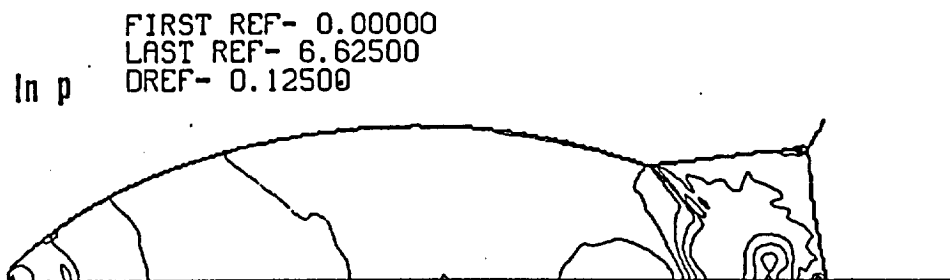
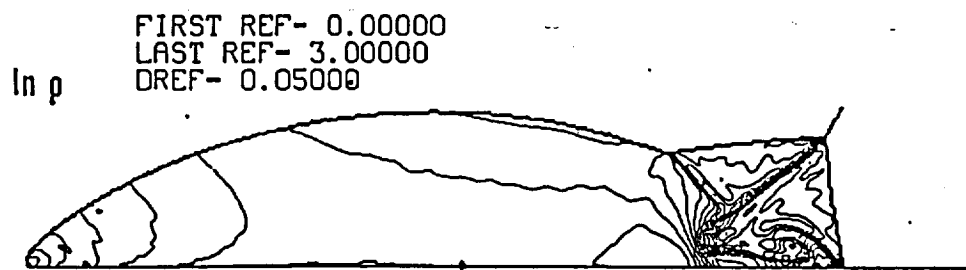


Fig. 30

successful shock-capturing code. Two movies have been made, showing the evolution of isomach patterns for this case; the first in real space, and the second in a self-similar mode.

Propagation of a circular shock

The second application of the code, using both x-shocks and y-shocks, is the analysis of the propagation of a circular shock into a gas at rest. We start with a prescribed circular shock, inside which speed of sound, velocity a modulus and entropy are constant (consistent with the shock strength), and the velocity vector is oriented radially. To avoid physical inconsistencies, an inner region is cut off from the flow field (ABCD in Fig. 38). This exercise has been performed solely to test the symmetry of the code in an axisymmetric problem, analyzed on a Cartesian grid. We did not try to preserve the axial symmetry of the core of the perturbed region; neither did we attempt to force the boundary conditions at the inner boundary to have a simple physical interpretation. The computational grid is Cartesian and the grid size is .005. The initial configuration of the shock is shown in Fig. 38. The segments issuing from the shock points (which are coded as in the previous exercise) are proportional to $M-1$ (where M is the shock Mach number) and their direction is the computed normal to the shock. Successive stages are shown in Figs. 39 through 41. The shock expands well and symmetry is preserved, for all practical purposes. A perfect symmetry is hard to achieve; for example, mesh crossings may occur at two successive steps for y-shocks in the upper or lower half of the figure, as a consequence of different round-off or truncation errors. This produces minor local losses of symmetry, which have to be reabsorbed over a few computational steps. We are not concerned with such imperfections; we are happy to see that they do not degenerate or create instabilities, and that the general trend is not affected by them.

Expansion from a duct into a large cavity

In the third application of the code, using both x-shocks and y-shocks, we analyze the flow produced when a normal shock, travelling in a straight duct, reaches the end of the duct and propagates into a gas at rest at constant pressure in an infinite cavity. As the flow expands around the rim of the duct, its pressure falls well below the ambient pressure. Along the wall of the cavity, thus, a sudden recompression must take place. Considering the Mach number of the expanded flow, which is at least 6.819, the recompression may occur only through a normal shock. In an inviscid model, a steady shock would decrease the total pressure to a value, far below the ambient pressure. Therefore, a recirculation initiates along the vertical wall of the cavity, and the flow separates at the rim, forming a plume. As the plume develops in length, a large

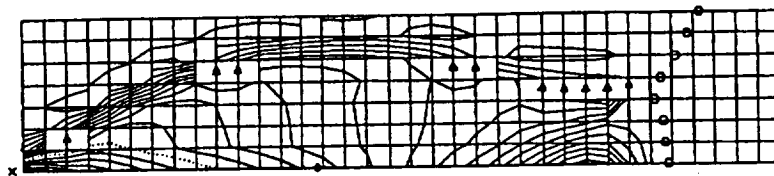


Fig. 31

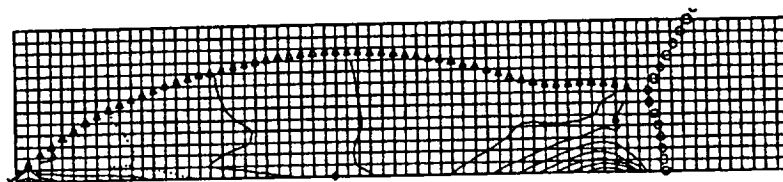


Fig. 32

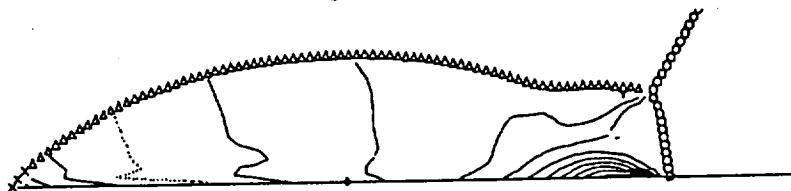


Fig. 33

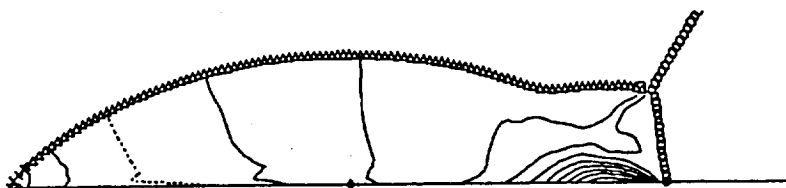


Fig. 34

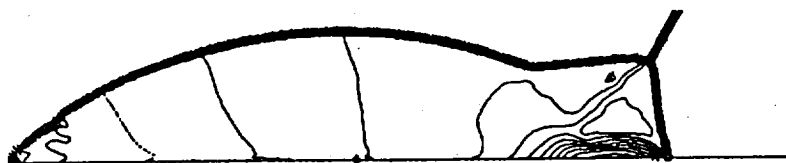


Fig. 35

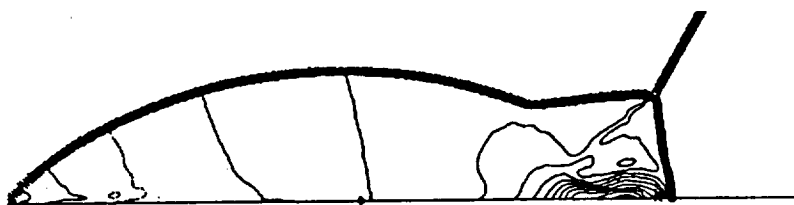


Fig. 36

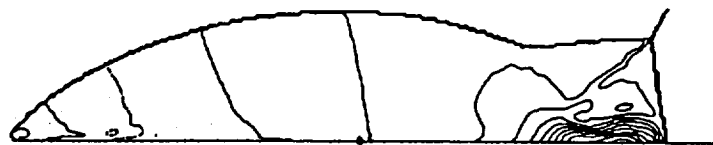


Fig. 37

vortex appears under it, and moves outwards. The vortex should eventually be carried away, leaving a dead water region near the wall and under the plume, at the same pressure as the original pressure in the cavity. The final shape of the plume should be consistent with the pattern computed under the assumption of steady flow, bounded by a constant pressure streamline issuing from the rim of the duct.

The shock Mach number is 2. Our calculation (on a basic Cartesian square grid with 200 intervals in either direction) may provide a description of the first phase of the expansion or a coarser analysis of the evolution of the flow over a longer period of time, by simply changing the number of intervals across the exit section of the duct. We used 7, 21 and 42 points across.

The first test was made against an experimental interferogram (Ref. 4, as quoted by Ref. 5), the main features of which are sketched in Fig. 42, top. Density contours, as computed by us, are shown in the other two parts of Fig. 42. The figure in the middle has been obtained using 21 points, and the one at the bottom using 42 points. The agreement, in both cases, is good. Using only 7 intervals across the duct, we can proceed farther in time; Figs. 43 and 44 show plots of isomachs at successive stages of evolution (steps 200 and 400). The presence of vortices is suggested by closed isomachs. To show the evolution of the vortices more clearly, we reproduce a couple of frames from a movie of streaklines (Figs. 45 and 46). Circles represent particles originally found in the cavity, when the gas was at rest; crosses represent particles issuing from the duct at regular intervals (every third computational step). The precursor shock, as it appears in the preceding figures, has been drawn here as a broken line. One can see the compression of the original particles behind the shock (weaker at the bottom, where the shock is merely an acoustic wave). The effect of the recompression shock in the plume is much stronger. The contact surface, separating the original gas from the gas issuing from the duct, is shown by the transition between circles and crosses. The large vortex under the plume expands and moves out, as anticipated. The density in the vortex is

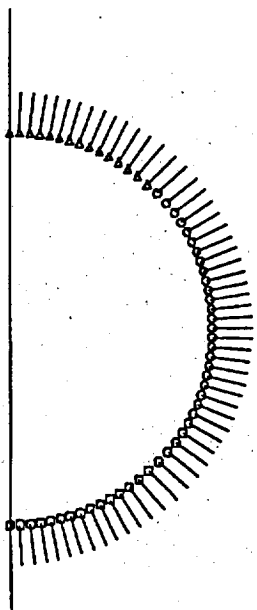


Fig. 38

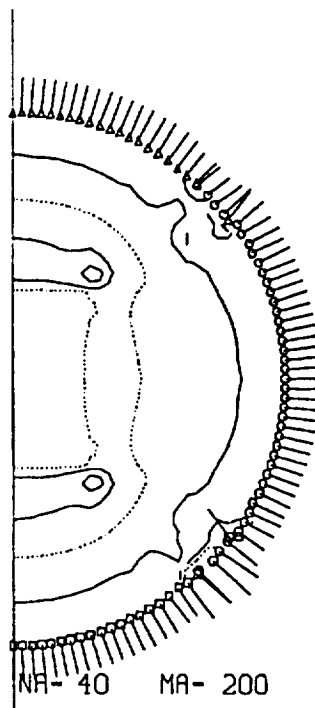


Fig. 39

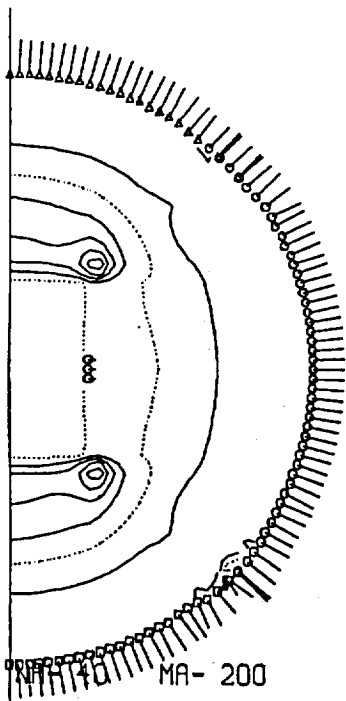


Fig. 40

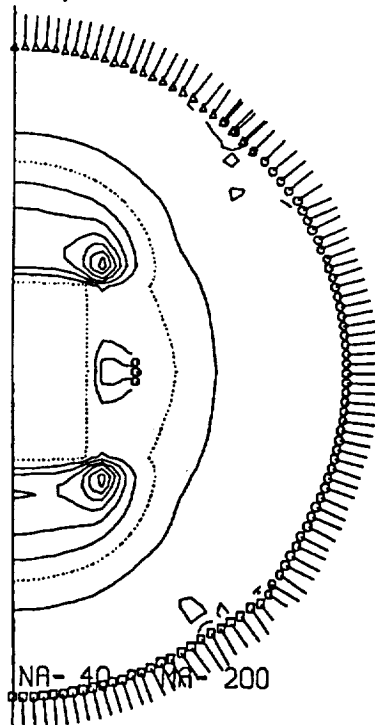


Fig. 41

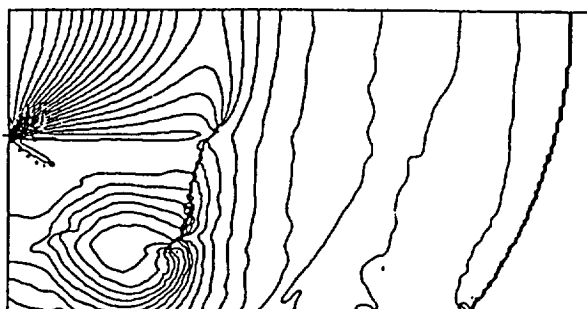
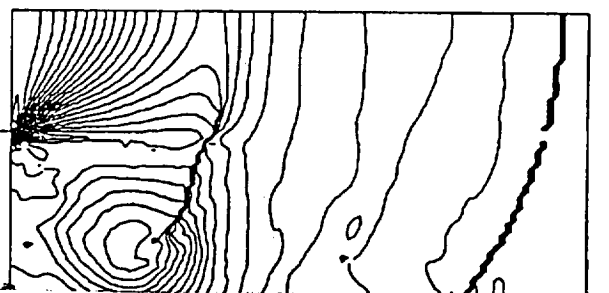


Fig. 42

very low, as the almost total absence of tracking particles reveals. This result is consistent with the isopycnic plots of Fig. 42. The isomach plots reveal the formation of the plume which, in its first portion, is practically stabilized. The slope of the plume edge is the same as the one evaluated by the steady state analysis, mentioned above. The plume edge is also evident in Figs. 45 and 46. As the calculation proceeds, a distant observer will not be able to distinguish between our plots and a plot of a theoretical inviscid plume, limited by a sharp contact discontinuity.

Transonic flow in a duct with a 180° bend

Finally, we analyze the flow produced by a shock, entering a curved duct with an original shock Mach number of 3. The shock is followed by a uniform supersonic flow ($M=1.6$), and we assume that the flow maintains its values at the entrance of the duct during the entire analysis. The duct itself is generated by conformal mapping from a rectangle, and a computational orthogonal grid is generated simultaneously, and it appears as in Fig. 47. In the example presented here, we use a 150x30 mesh for the calculation.

As the shock is about to penetrate the region of highest curvature (Fig. 48), a slight recompression follows it near the inner wall, in turn followed by an expansion (the latter being the obvious consequence of the duct geometry acting on a supersonic flow). Later on (Fig. 49) the expansion and recompression become stronger; part of the shock near the inner wall is followed by a subsonic flow. The shock itself cannot remain orthogonal to the outer wall; neither can it afford a regular reflection. A Mach stem originates, followed by a short reflected shock, almost parallel to the outer wall.

In Fig. 50, we see a bigger subsonic region, which is now following the longer portion of the original shock. The reflected shock is much longer, and a recompression shock appears to terminate the strong supersonic expansion near the inner wall.

The shock pattern in Fig. 51 clearly reveals shocks of different natures. First, we see what is left of the original shock, and a Mach stem of increased length. The reflected shock stemming from the triple point has become very long and is pushed towards the inner wall by the high-pressure region produced by the curvature of the outer wall. The recompression shock has also grown in length; so much, that it starts interfering with the reflected shock. Inspection of the velocities shows that a small reverse-flow region is present in the high-pressure zone behind the recompression shock.

The evolution continues in Fig. 52, where we see the reflected shock on the verge of hitting the inner wall. Part of

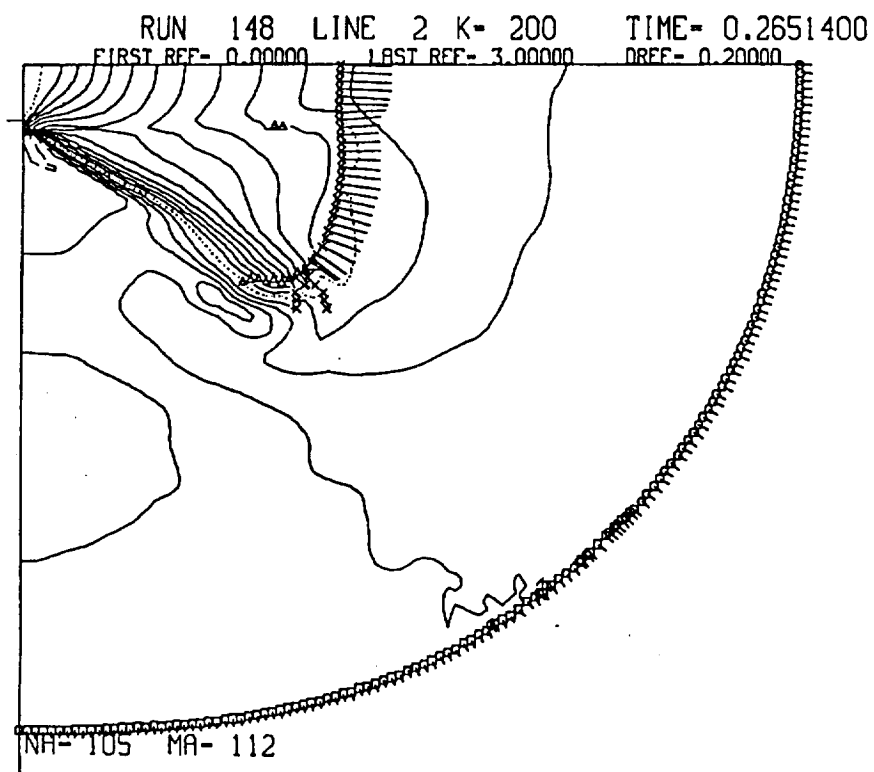


Fig. 43

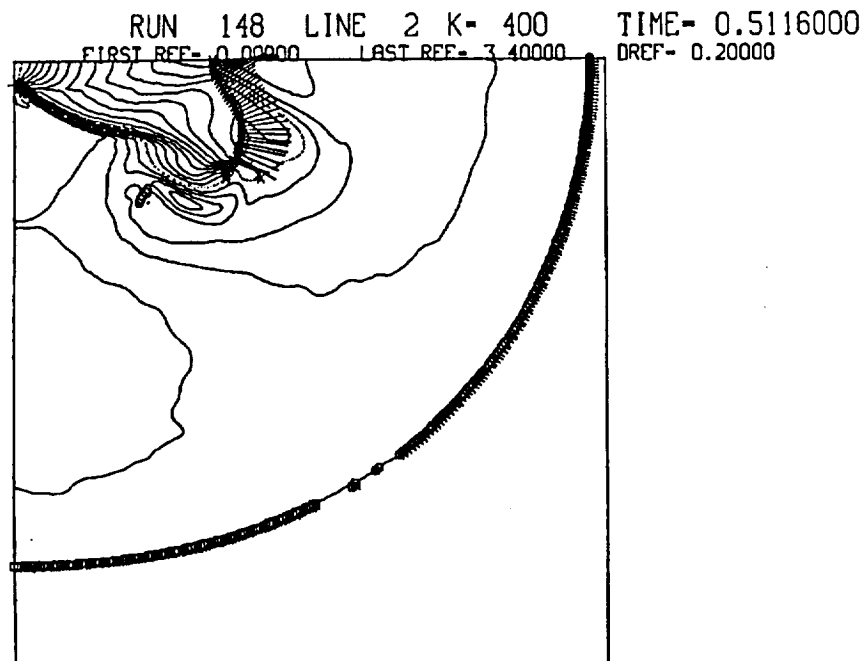


Fig. 44

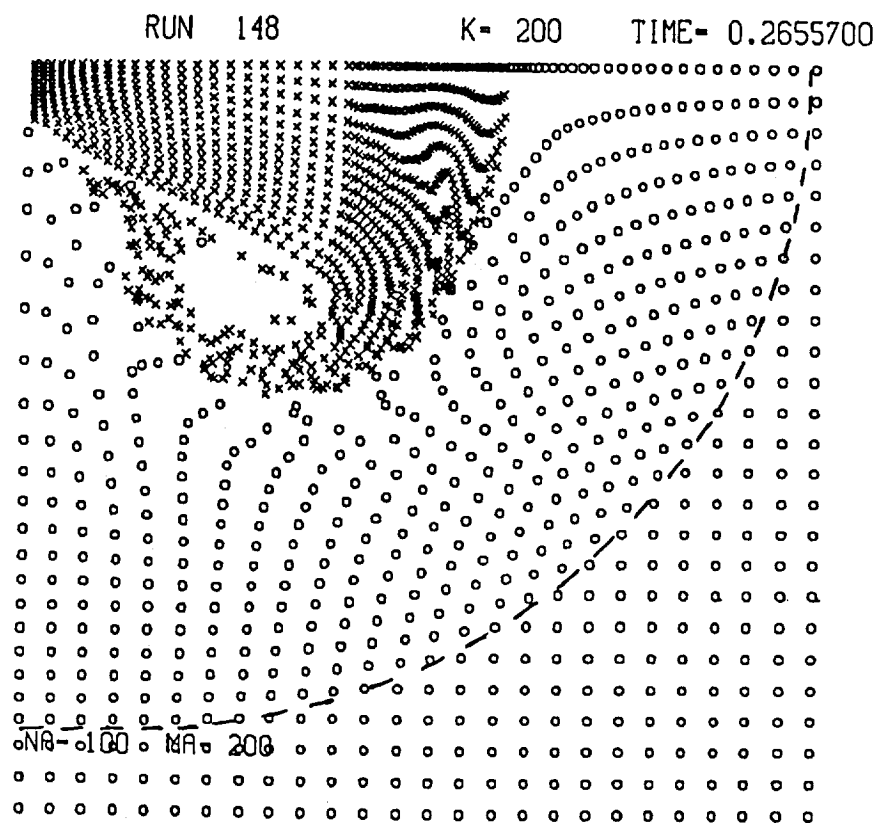


Fig. 45

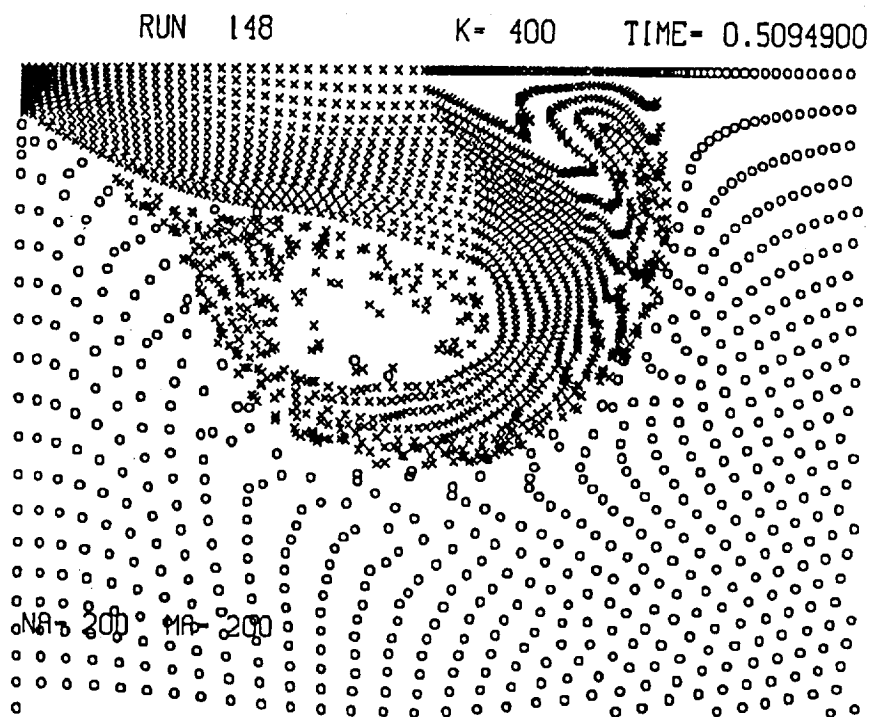


Fig. 46

it, distorted, merges with the recompression shock and becomes the limiter of the supersonic region. In Figs. 53 and 54, isobars and isentropic lines are shown, after removing the symbols for the shocks. From Fig. 53 it is evident that the highest pressure is on the outer wall of the elbow; pressures below the value in the gas at rest are denoted by dotted lines. It is also important to note that the original shock has lost most of its strength, whilst the Mach stem is becoming more important. The same conclusion can be drawn from Fig. 54. Indeed, the entropy jump across the Mach stem is about the same as it was across the initial shock (the highest entropy value behind the Mach stem equal the constant value in the oncoming flow). The oncoming flow itself is steady and isentropic; the particles which underwent the strong isentropic expansion near the inner wall are violently recompressed, and this produces the dark region of very high entropy, visible in Fig. 54.

The last phase of the evolution begins as shown in Fig. 55. The Mach stem keeps growing, and the original shock is reduced to a negligible strength. The reflected shock bounced back from the inner wall and burst into three parts. The first is still attached to the triple point; the second seems to hang from the inner wall; both have practically lost all strength. The third part became part of the steady recompression shock. Note again the entropy distribution in Fig. 56, for which the above comments can be repeated. Finally, the Mach stem ends spanning the entire duct and assumes the role played by the original shock. The flow in the elbow becomes steady, with the recompression shock playing the same role as the embedded shock on a transonic airfoil; its strength is very high near the inner wall, and it tapers down to zero somewhere in the middle of the duct. As a consequence of the entropy losses, the outgoing shock is no longer as strong as the original shock (Fig. 57).

CONCLUSIONS

The numerical experiments performed so far on a variety of problems, with different geometries, flow conditions and mesh resolutions (samples of which were presented above) seem to prove that our technique combining the λ -scheme with shock-fitting is accurate, fast and robust. The shaping of the shock-fitting code into a "black box" allows it to be used to analyze flows very different in nature, without requiring special recordings. The entire technique is, thus, very simple and easy to apply. We consider our work on two-dimensional flow practically concluded, and we anticipate the possibility of extending the technique to three-dimensional, unsteady flows

without major variations.

References

1. Moretti, G., A technique for integrating two-dimensional Euler equations, *Comp. and Fluids*, 15:59-75, 1987
2. Proceedings of the GAMM Workshop, Rocquencourt, June 1986, to be published by Vieweg Publ., 1987
3. Woodward, P. and Colella, P., The numerical simulation of two-dimensional fluid flow with strong shocks, *J. Comp. Phys.* 54:115-173, 1984
4. Mandella, M. and Bershader, D., Quantitative study of the compressible vortices: Generation, structure and interaction with airfoils, AIAA Paper 87-0328, 1987
5. Moon, Y.J. and Yee, H.C., Numerical simulation by TVD schemes of complex shock reflections from airfoils at high angle of attack, AIAA Paper 87-0350, 1987

Acknowledgements

The present Report summarizes the current stage of evolution of a general technique for shock-fitting in two space dimension and time. The evolution has been slow and many steps were taken that were successively retraced. Minor and major changes of mind occurred. In the difficult task of moving from simple to complex problems and from ad-hoc codes to general codes, testing the soundness of the logic, the robustness of the programs and the physical realism of results, we have been exploiting the skill and dedication of a number of people, to whom we extend our warmest thanks:

Miss Catherine Fahy, from our organization,
Prof. Luca Zannetti, Politecnico di Torino, Italy,
Prof. Maurizio Di Giacinto, Prof. Marcello Onofri and Dr. Mauro Valorani, University of Rome, Italy,
Dr. George Vradis, Polytechnic University, Farmingdale, NY.

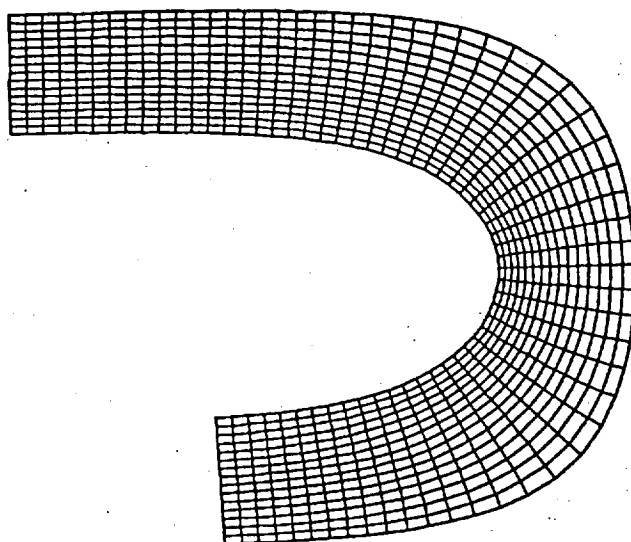


Fig. 47

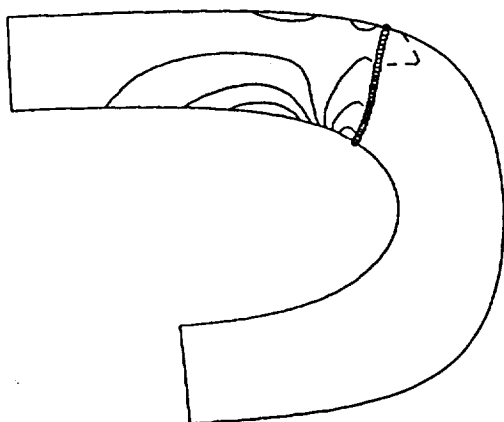


Fig. 48

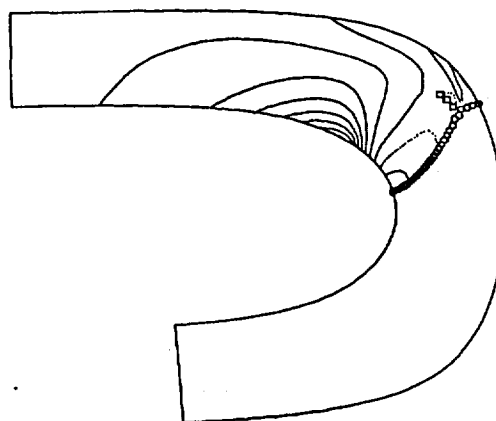


Fig. 49

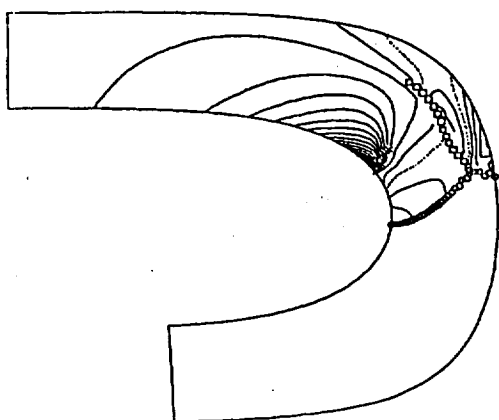


Fig. 50

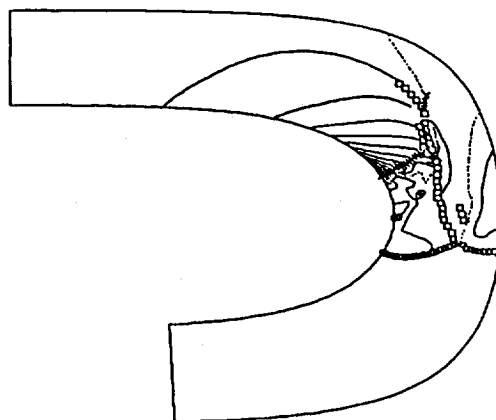


Fig. 51

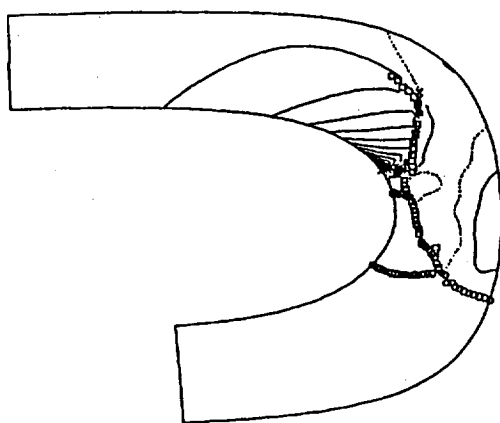


Fig. 52

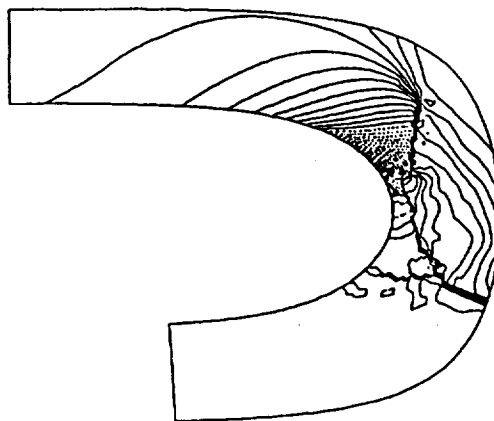


Fig. 53

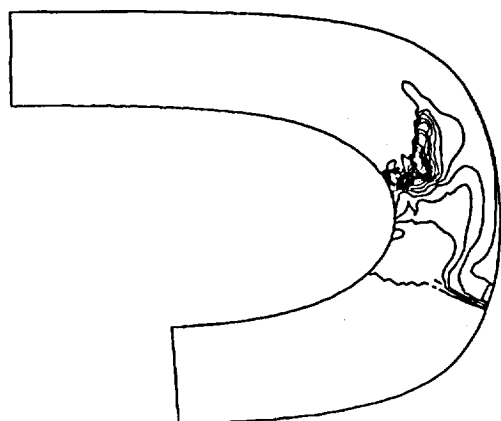


Fig. 54

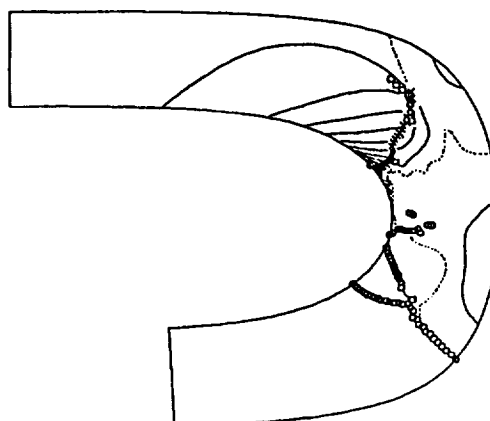


Fig. 55

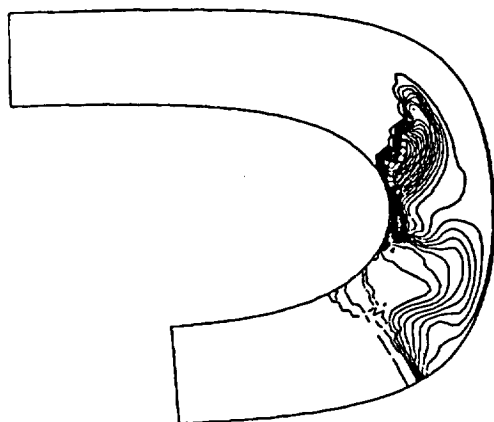


Fig. 56

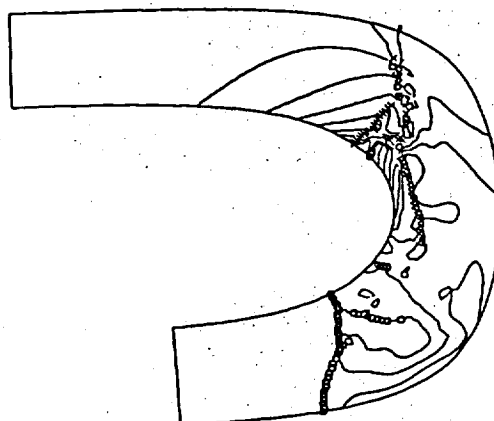


Fig. 57